



Contents lists available at ScienceDirect

Optik

journal homepage: www.elsevier.com/locate/ijleo

Original research article

Influence of random aspheric parameter errors on the wavefront deformation for segmented primary mirror and its correction

Huisheng Yang^{a,b,*}, Xuejun Zhang^a, He Bao^a, Xiaokun Wang^a, Fangmao Chai^a^a Changchun Institute of Optics, Fine Mechanics and Physics, Chinese Academy of Sciences, Changchun 130033, China^b University of Chinese Academy of Sciences, Beijing 100049, China

ARTICLE INFO

Keywords:

Ultra large aperture
Space-based telescope
Segmented primary mirror
Aspheric parameter errors
Wavefront deformation

ABSTRACT

Segment random aspheric parameter errors will generate uncertain wavefront deformation which can be effectively compensated using segment pose alignment. We propose the linear sensitivity matrix of the wavefront deformation originating from the errors through ray tracing, and deduce the prediction formula of the deformation. The correction and prediction methods using segment pose adjustment to compensate the errors are presented. Numerical simulations results reveal that both the mean square wavefront deformations before and after compensation can be perfectly predicted with the prediction errors of the expectation less than $\pm 2\%$ and of the variance less than $\pm 5\%$.

1. Introduction

Future and present science targets keep driving the desire for the development of telescope aperture for greater light-gather power and spatial resolution, to explore and study more distant and faint planet [1,2]. The study from National Aeronautics and Space Administration (NASA) shows that the telescope aperture should be larger than 8 m to meet the basic requirements of astronomy observation [3,4]. However, the carrying capacity of the launch vehicle is limited. The space telescope must be designed according to the launch vehicle. At present, telescopes using segmented primary mirror (PM) become the best choice for space-based observatories with aperture size more than 4 m [5–7]. For examples, the James Webb Space Telescope (JWST) [8], the Advanced Technology Large Aperture Space Telescope (ATLAST) [9] and the Thirty Meter Space Telescope (TMST) [10] are all segmented telescopes.

Segmented mirrors need to be correctly phased, which is defined as co-phasing, to achieve the imaging capability equivalent to a monolithic mirror [11]. At present, the research on segment co-phasing mainly focuses on the error detection [12–15], and the impacts of piston and tip/tilt errors with definite value [16–22]. However, the correct prescription (aspherical parameters) of segments are the prerequisite for co-phasing. The segment prescription errors can lead to significant co-phasing errors even though the segments locate in correct positions. But, the research on prescription errors is rarely concerned. This is because the prescription errors are random, the fabrication of segments with diameter large than 1 m needs exorbitant fabrication cost and processing cycle, and it is impossible to analyze the impact of prescription errors by manufacturing lots of segments. However, this subject is very significant, which can reasonably allocate the segment fabrication tolerance to ensure that the prescription of segments meet the co-phasing requirement, and can evaluate the overall development difficulty of the segmented PM at the initial stage of the optical system.

This paper proposes a method for predicting the mean square of wavefront deformations (WD) produced by random prescription

* Corresponding author at: Changchun Institute of Optics, Fine Mechanics and Physics, Chinese Academy of Sciences, Changchun 130033, China.
E-mail address: yanghuisheng@126.com (H. Yang).

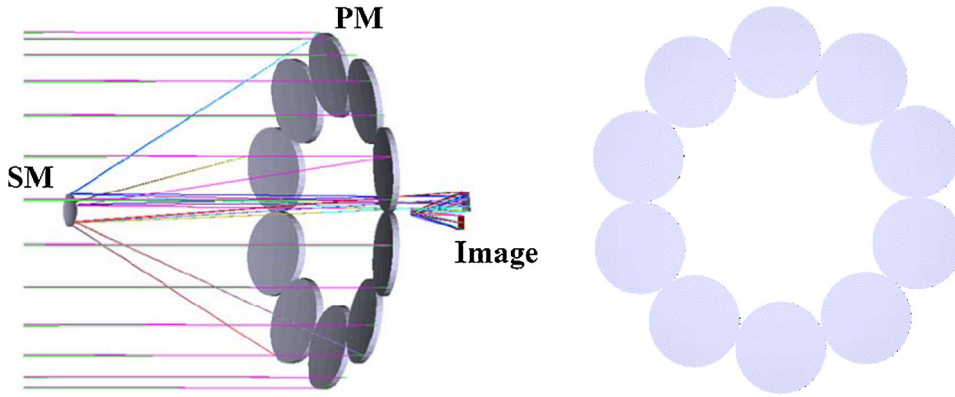


Fig. 1. Optical design of an 8 m space telescope.

errors before and after compensation. Firstly, we introduced the basic composition of a segmented PM with 8 m aperture and analyze the sources of segments prescription errors. The linear sensitivity matrix of the WD to segments prescription errors is then presented, the prediction formula of the WD mean square is deduced, and Monte Carlo simulations are achieved to verify the validity of the prediction. Finally, we propose a method for compensating the WD using segments pose adjustment (including position adjustment and attitude adjustment), and deduce the prediction formula of the WD mean square after compensation, which is also verified by numerical simulations. This works can provide a theoretical basis and data support for segmented telescope design and fabrication.

2. Segmented primary mirror architecture and the source of the prescription errors

The segmented PM is illustrated in Fig. 1. It is composed of 10 individual silicon carbide (SiC) mirror segments. When properly phased relative to each other, these segments act as a single mirror which can provide an aperture of approximate 8 m for the observatory. Each segment is circular, 1.9 m in diameter, and has identical prescription (radius of curvature 10 m and conic constant -1), which can effectively reduce the fabrication difficulty and improve manufacturing efficiency. These segments are centrosymmetrically distributed on a ring of 6.1 m in diameter, and phased via 6 degree of freedom (DOF) segments rigid body motions.

Segments are grinded, ground and polished successively to obtain the optical surface meeting requirements. Different testing methods are used in different stages to ensure machining accuracy. Interference testing is used in the polishing stage, and profilometer testing was used in other stages. Segment prescription errors mainly originate from test errors in manufacturing, as the manufacturing precision is greater than the corresponding testing accuracy. The prescription errors are mainly produced in profilometer testing, because the material removal is so little in polishing process that it cannot change segment surface-shape. The profilometer testing consists of two stages. Firstly, the coordinate values of discrete points on the segment surface are measured, and then aspheric parameters are calculated using least square method. Therefore, the prescription error is the function of the measurement errors of all the points. According to the central limit theorem (CLT), the segment prescription errors approximately follow multidimensional independent normal distribution:

$$\begin{aligned} \Delta R &\sim N(0, \sigma_R) \\ \Delta k &\sim N(0, \sigma_k) \end{aligned} \tag{1}$$

3. Wavefront deformation originating from the prescription errors

3.1. Basic theory

According to the geometric ray-trace optics, the optical path length (OPL) of an incident-ray reflected by a mirror is the function of the surface-shape, the mirror position and attitude, as well as the position and direction of the incident-ray:

$$OPL = f(R, k, s, \theta, \hat{i}, p) \tag{2}$$

where R is the paraxial radius of curvature. k is the conic constant. s is the segment position vector. θ is the segment attitude vector. \hat{i} is the unit direction vector of the incident-ray. p is the position vector of the incident-ray.

According to the function error transfer theory, the optical path difference (OPD) produced by slight aspheric prescription errors ΔR and Δk can be expressed as:

$$OPD = \frac{\partial f}{\partial R} \Delta R + \frac{\partial f}{\partial k} \Delta k \tag{3}$$

where $\partial f / \partial R$ and $\partial f / \partial k$ are error transfer coefficients.

A conic section is the locus of all points P whose distance to a fixed point F is a constant multiple of the distance from P to a fixed

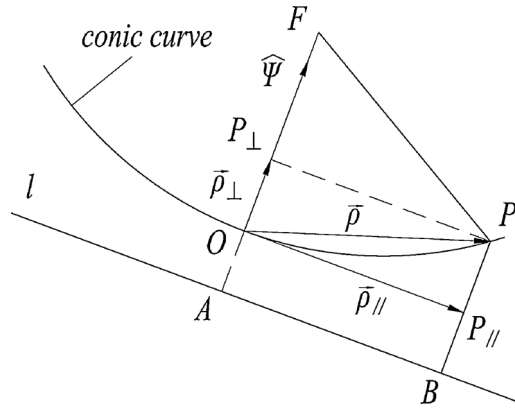


Fig. 2. The coordinate-free conic curve.

line l (Fig. 2). We obtain an ellipse for $0 < e < 1$, a parabola for $e = 1$, and a hyperbola for $e > 1$. Therefore, the coordinate-free formula of the conic-section-of-revolution surface used in segmented PM is obtained:

$$\vec{\rho}^T (\mathbf{I} - e^2 \hat{\psi} \hat{\psi}^T) \vec{\rho} - 2f(1 + e) \hat{\psi} \cdot \vec{\rho} = 0 \tag{4}$$

where F is the focus of the conic. e is the eccentricity. l is the directrix of the conic. f is the distance from the conic vertex O to the focus F . $\hat{\psi}$ is principle axis vector of the PM from the vertex to the focus. $\vec{\rho}$ is the vector from O to P . \mathbf{I} is a unit matrix. It can be easily obtained:

$$k = -e^2; R = f(1 + e) \tag{5}$$

The incident-ray with direction \hat{i} originating at point P_{in} intersects the optical surface at point P (reflection point), and then the vector $\vec{\rho}$ defined by the mirror vertex can be expressed as (Fig. 3):

$$\vec{\rho} = \vec{p} + L\hat{i} \tag{6}$$

where \vec{p} is the position vector of point P_{in} defined by the vertex and L is the distance from point P_{in} to point P .

It can be obtained from Eqs. (4)–(6):

$$AL^2 + BL + C = 0 \tag{7}$$

define surface dyadic $\mathbf{M} = \mathbf{I} + k\hat{\psi}\hat{\psi}^T$, and the coefficients can be written as :

$$A = \hat{i}^T \mathbf{M} \hat{i}$$

$$B = 2\hat{i}^T (\mathbf{M}^T \vec{p} - R\hat{\psi})$$

$$C = \vec{p}^T (\mathbf{M} \vec{p} - 2R\hat{\psi})$$

For $A \neq 0$, the solution of Eq. (7) is:

$$L = \frac{-B \pm \sqrt{B^2 - 4AC}}{2A} \tag{8}$$

When the optical surface is concave, the Eq. (8) takes a positive sign, otherwise it takes a negative sign. Partial derivatives of A , B and C are:

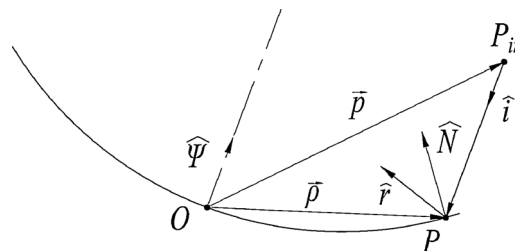


Fig. 3. An incident-ray is reflected by a mirror with a conic-section surface.

$$\begin{aligned}
 \frac{\partial A}{\partial R} &= 0 & \frac{\partial A}{\partial k} &= \hat{\mathbf{i}}^T \hat{\boldsymbol{\psi}} \hat{\boldsymbol{\psi}}^T \hat{\mathbf{i}} \\
 \frac{\partial B}{\partial R} &= -2\hat{\mathbf{i}}^T \hat{\boldsymbol{\psi}} & \frac{\partial B}{\partial k} &= 2\hat{\mathbf{i}}^T \hat{\boldsymbol{\psi}} \hat{\boldsymbol{\psi}}^T \vec{\mathbf{p}} \\
 \frac{\partial C}{\partial R} &= -2\vec{\mathbf{p}}^T \hat{\boldsymbol{\psi}} & \frac{\partial C}{\partial k} &= \vec{\mathbf{p}}^T \hat{\boldsymbol{\psi}} \hat{\boldsymbol{\psi}}^T \vec{\mathbf{p}}
 \end{aligned} \tag{9}$$

Set: $D = \sqrt{B^2 - 4AC}$, and the sensitivity of the distance L to prescription errors can be expressed by the partial derivatives of A, B and C.

For the concave optical surface:

$$\frac{\partial L}{\partial R} = \frac{B - D}{2AD} \frac{\partial B}{\partial R} - \frac{1}{D} \frac{\partial C}{\partial R} \tag{10}$$

$$\frac{\partial L}{\partial k} = \frac{1}{2A} \left(\frac{B}{D} - 1 \right) \frac{\partial B}{\partial k} - \left(\frac{C}{AD} + \frac{D - B}{2A^2} \right) \frac{\partial A}{\partial k} - \frac{1}{D} \frac{\partial C}{\partial k} \tag{11}$$

And the convex optical surface:

$$\frac{\partial L}{\partial R} = \frac{-B - D}{2AD} \frac{\partial B}{\partial R} + \frac{1}{D} \frac{\partial C}{\partial R} \tag{12}$$

$$\frac{\partial L}{\partial k} = -\frac{1}{2A} \left(1 + \frac{B}{D} \right) \frac{\partial B}{\partial k} + \left(\frac{C}{AD} + \frac{B + D}{2A^2} \right) \frac{\partial A}{\partial k} + \frac{1}{D} \frac{\partial C}{\partial k} \tag{13}$$

When A gets close to 0, partial derivatives obtained by Eqs. (10)–(13) will have nonnegligible errors. This is because the denominator approaching 0 infinitely amplifies the rounding error. Especially for $A = 0$, the rounding error is infinity, which does not have a meaning. In order to solve this problem, we calculate the partial derivatives using linear interpolation during $A \in [-\epsilon, \epsilon]$. ϵ is a positive real number close to 0, and typically $1e-4$.

Differentiate Eq. (6), and the perturbation of the vector $\vec{\rho}$ can be expressed as:

$$d\vec{\rho} = \hat{\mathbf{i}} \cdot dL \tag{14}$$

The effect of prescription errors ΔR and Δk on the OPD can be seen in Fig. 4.

The solid curve in Fig. 4 is nominal surface, and the dashed line is actual surface with prescription errors. According to the Redding formulations [23], the total OPD is the sum of the changes in the incident-ray and reflected-ray path lengths:

$$OPD = dL_i + dL_r \tag{15}$$

The incident-ray OPD is the magnitude of the vector dL_i :

$$dL_i = -\frac{\hat{N}}{\hat{\mathbf{i}} \cdot \hat{N}} \cdot d\vec{\rho} \tag{16}$$

The reflected-ray OPD is the change in the incident-ray path length projected onto the reflected ray:

$$dL_r = -dL_i \cdot \hat{\mathbf{i}} \cdot \hat{\mathbf{r}} \tag{17}$$

The OPD due to the paraxial radius of curvature error is:

$$\frac{\partial OPD}{\partial R} = (\hat{\mathbf{i}} \cdot \hat{\mathbf{r}} - 1) \frac{\partial L}{\partial R} \tag{18}$$

The OPD due to the conic constant error is:

$$\frac{\partial OPD}{\partial k} = (\hat{\mathbf{i}} \cdot \hat{\mathbf{r}} - 1) \frac{\partial L}{\partial k} \tag{19}$$

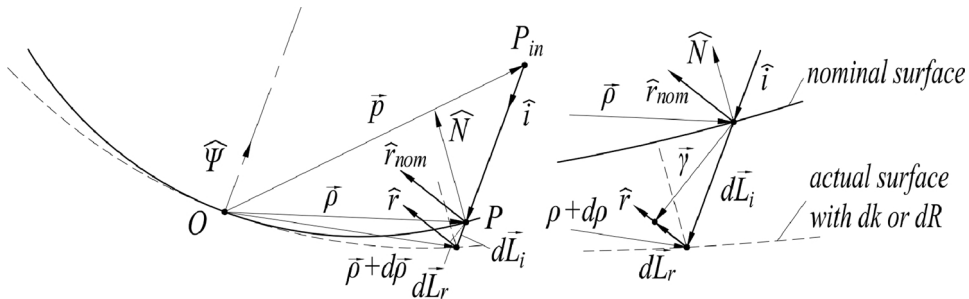


Fig. 4. WD originating from prescription errors.

Therefore, the OPD of the incident-ray i caused by prescription errors can be written as:

$$OPD_i = \begin{bmatrix} \frac{\partial OPD_i}{\partial R} & \frac{\partial OPD_i}{\partial k} \end{bmatrix} \begin{bmatrix} \Delta R \\ \Delta k \end{bmatrix} \tag{20}$$

The WD can be obtained by tracing all incident-rays using Eq. (20):

$$\Delta w = \begin{bmatrix} OPD_1 \\ \vdots \\ OPD_i \\ \vdots \\ OPD_{n \times m} \end{bmatrix} = S \Delta \tag{21}$$

where S is the linear sensitivity matrix of $n \times 2m$ (n is the quantity of incident-rays through one segment and m is the quantity of segments). Δ is a vector of $2m \times 1$ consisting of all the segments prescription errors.

3.2. Wavefront deformation prediction

Prescription errors follow multidimensional independent normal distribution, the expectations of which are zero. Therefore, the expectation of WD originating from prescription errors is also zero:

$$E(\Delta w) = SE(\Delta) = 0 \tag{22}$$

The variance of WD originating from prescription errors can be written as:

$$RMS^2 = \frac{1}{n} \Delta w^T \Delta w = \frac{1}{n} \xi^T Q \xi \tag{23}$$

where $Q = G^T G$, $G = S \text{diag}(\sigma)$, $\xi = \text{diag}(1/\sigma)\Delta$, σ is a vector composing of the standard deviations of Δ .

Q is a symmetric matrix and can be decomposed as:

$$Q = U^T \Sigma U \tag{24}$$

where U is an orthogonal matrix composed of the eigenvectors of Q and Σ is a diagonal matrix composed of the eigenvalue of Q .

Let $\xi' = U\xi$. Therefore, ξ' follows multidimensional independent normal distribution with a unit variance, and Eq. (23) can be written as:

$$RMS^2 = \frac{1}{n} \xi'^T \Sigma \xi' = \frac{1}{n} \sum_{i=1}^r \lambda_i \xi_i'^2 \tag{25}$$

$\xi_i'^2$ follows a chi-square distribution with one degree of freedom. The expectation and variance of WD RMS^2 are:

$$E(RMS^2) = \frac{1}{n} \sum_{i=1}^r \lambda_i \tag{26}$$

$$D(RMS^2) = \frac{2}{n^2} \sum_{i=1}^r \lambda_i^2 \tag{27}$$

where r is the rank of Q , n is the quantity of incident-rays. λ_i is the eigenvalue of Q .

The WD RMS^2 is a linear combination of independent chi-square distributions with one degree of freedom. According to Ref. [24], an approximate expression of this RMS^2 distribution is

$$RMS^2 \sim a\chi^2(b) \tag{28}$$

where the chi-square coefficient a and degree of freedom b can be expressed by the expectation and variance of WD RMS^2 :

$$a = \frac{D(RMS^2)}{2E(RMS^2)}; \quad b = \frac{2E(RMS^2)^2}{D(RMS^2)} \tag{29}$$

3.3. Numerical simulation

Monte Carlo simulations are performed to verify the conclusion deriving from Eq. (26) and Eq. (27). We trace 1037 uniformly distributed incident-rays on each segment surface of 1.9 m in diameter, calculate the OPD of all 10370 incident-rays reflected by the segmented PM using Eq. (20), and obtain the total WD stemming from segments prescription errors by Eq. (21). The simulation results sampling 100,000 times are plotted in Fig. 5. Fig. 5(a) is the WD RMS^2 probability distribution, where the standard deviations of each segment prescription errors (ΔR or Δk) are the same, and can lead to one square wavelength WD RMS^2 . It can be seen from the probability distribution that the WD RMS^2 approximately follows a chi-square distribution. Fig. 5(b) shows the average WD map. Because positive OPD compensates negative OPD, the map RMS is approximately zero, which is consistent with Eq. (22). Moreover,

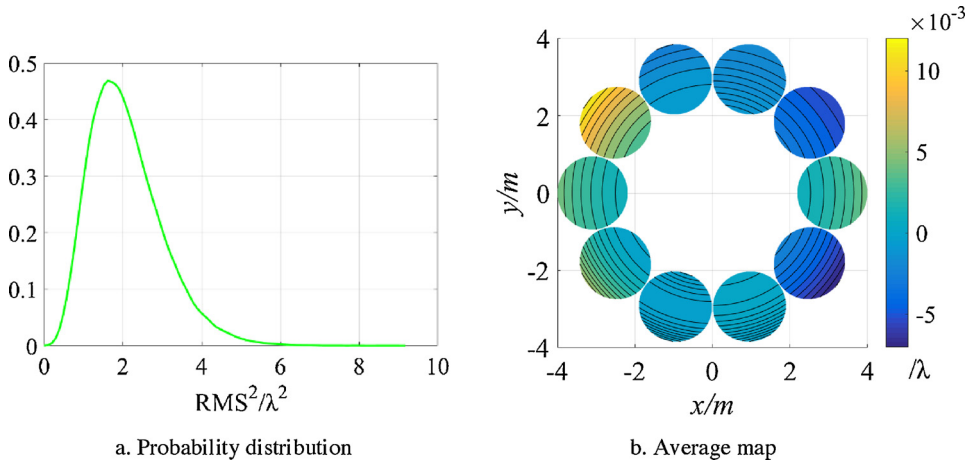


Fig. 5. The WD originating from normal distribution prescription errors.

the RMS^2 expectation and variance obtained by Monte Carlo simulations are $(1.4482\lambda)^2$ and $(0.9613\lambda)^4$ respectively, which are consistent with the prediction results $(1.4477\lambda)^2$ and $(0.9618\lambda)^4$ deriving from Eqs. (26) and (27).

In order to further verify the validity of Eqs. (26) and (27), we establish segmented PM models using different parameters, calculate the RMS^2 caused by prescription errors with different standard deviations, and compare the results of Monte Carlo simulations with predictions. Fig. 6 plots the 100 times verification results for a segmented PM with 8 m aperture. Each verification is completed using the following parameters: the Monte Carlo sampling times 100,000, the paraxial ROC R randomly taking value between 8 m and 15 m, the conic constant k randomly taking value between -2 and 2, the segment quantity m randomly taking value between 2 and 10, the segment diameter seg_D randomly taking value between 1 m and 1.9 m, the standard deviation of ΔR randomly taking value between 0 and 1.38 mm and the standard deviation of Δk randomly taking value between 0 and 4.68e-3. The plots indicate that the prediction errors of the RMS^2 expectation and variance are less than $\pm 2\%$ and $\pm 5\%$ respectively.

4. Prescription errors correction

4.1. Basic theory

The WD originating from segments prescription errors is defocus in PM coordinate system, but piston, tip/tilt, defocus and coma in segment coordinate system. It can be partially corrected by segment pose adjustment. The sensitivity of the WD Δw_p to segment pose changes defined in segment coordinate system can be written as:

$$\Delta w_p = A_{ip} \Delta X \tag{30}$$

where A_{ip} is the sensitivity matrix and ΔX is the segment pose perturbations vector.

The correction error E is defined as the sum of the square deviation between the WD originating from segment prescription errors and the WD stemming from segment pose changes:

$$E = \sum_{i=1}^n (\Delta w_i - \Delta w_{pi})^2 \tag{31}$$

According to the least square method theory, the minimum correction WD can be obtained when the segment moves to the best-

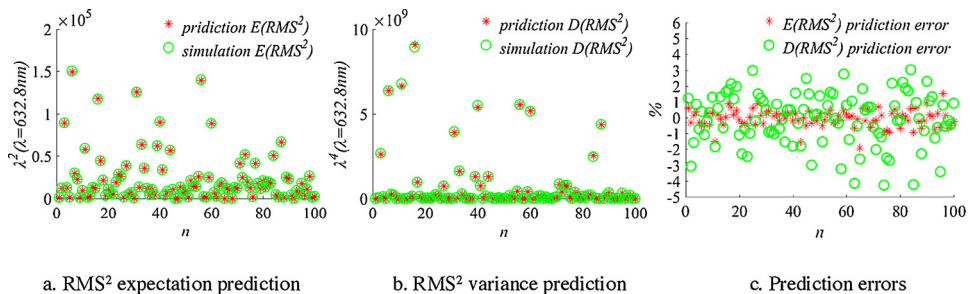


Fig. 6. Verification results of 100 random sampling for WD originating from different prescription errors of segmented PMs with disparate parameter.

fitting position:

$$\Delta X = (A_{ip}^T A_{ip})^{-1} A_{ip}^T \Delta w \tag{32}$$

The WDs produced by pose changes θ_x and δ_y are similar, as well as that by pose changes θ_y and δ_x , which can lead to singular base function matrix. Therefore, the corrections are accomplished in two stages: firstly using base functions composed of pose changes θ_x , θ_y , θ_z and δ_z , and secondly using θ_z , δ_x , δ_y and δ_z , compensate the segment prescription errors.

4.2. Prediction of residual wavefront deformation

Set the residual WD Δw_r as $\Delta w_{residuals}$, and we have:

$$\Delta w_r = \Delta w - \Delta w_{ip} \tag{33}$$

Simultaneous Eqs. (21), (30), (32), (33), can obtain:

$$\Delta w_r = B \Delta \tag{34}$$

where $B = S - A_{ip} (A_{ip}^T A_{ip})^{-1} A_{ip}^T S$.

Using the derivation process similar to Section 3.2, we can obtain the predictions of residual WD RMS^2 are:

$$E(RMS^2) = \frac{1}{n} \sum_{i=1}^r \lambda_i \tag{35}$$

$$D(RMS^2) = \frac{2}{n^2} \sum_{i=1}^r \lambda_i^2 \tag{36}$$

where r is the rank of \mathbf{Q} . n is the quantity of incident-rays. λ_i is the eigenvalue of \mathbf{Q} , $\mathbf{Q} = G^T G$. $G = [A - A_{ip} (A_{ip}^T A_{ip})^{-1} A_{ip}^T A] \text{diag}(\sigma)$. σ is a vector composed of the standard deviations of all segments prescription errors.

4.3. Numerical simulation

Fig. 7 shows the WDs originating from definite prescription errors before and after correction. Where, the paraxial radius of curvature error ΔR is 10.7λ ($\lambda = 632.8nm$), which can produce 1λ WD RMS, and the conic constant error Δk is $2.3e-5$, which can also produce 1λ WD RMS. Because the WDs stemming from ΔR and Δk can compensate each other, the WD RMS before correction does not follow the root sum square (RSS) law, is only 0.2296λ , which can be corrected to 0.0725λ via the first correction, and to 0.0724λ by the second correction. The contributions of each DOF pose adjustment are shown in Table 1.

It can be seen from Table 1 that the WD caused by definite prescription errors can be corrected by segment motions of θ_x , θ_y , θ_z and δ_z . The rotation θ_y has the highest contribution, and corrects nearly 87% WD. The rotation θ_x and θ_z have little contributions, and can be ignored.

In order to further verify the validity of the correction method, we simulate a correction of WD produced by segment with different prescription errors. The WDs before and after correction are shown in Fig. 8. where each segment prescription error is produced by random sampling, which is not known in advance. Comparing the figure before and after the correction, it can be found that the segment pose can effectively compensate the segment prescription errors, but it should also be noticed that this correction is incomplete. To further correct the residual WD, it is necessary to change the segment surface-shape using active optics.

In order to verify the prediction method of the residual WD, numerical simulations using the same setting as that in Fig. 6 are achieved. Fig. 9 shows the 100 times simulation results, which indicate that the prediction errors of RMS^2 expectation and variance

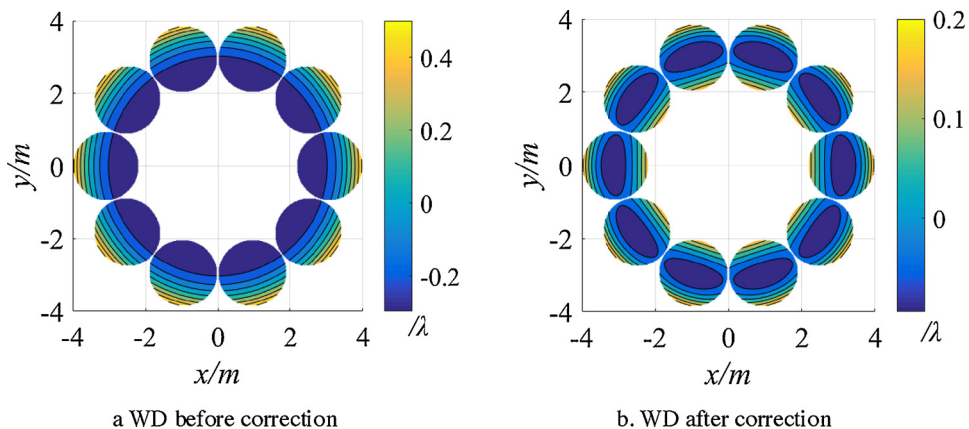


Fig. 7. Correction of the WD originating from segment with uniform prescription errors.

Table 1

Contributions of each segment DOF for the correction of WD originating from definite prescription errors.

WD	θ_x	θ_y	θ_z	δ_x	δ_y	δ_z
RMS/ λ	3.7e-9	0.2	1.5e-9	/	/	7.9e-2
RMS/ λ	/	/	6.7e-14	1.3e-3	6.7e-15	3.5e-5

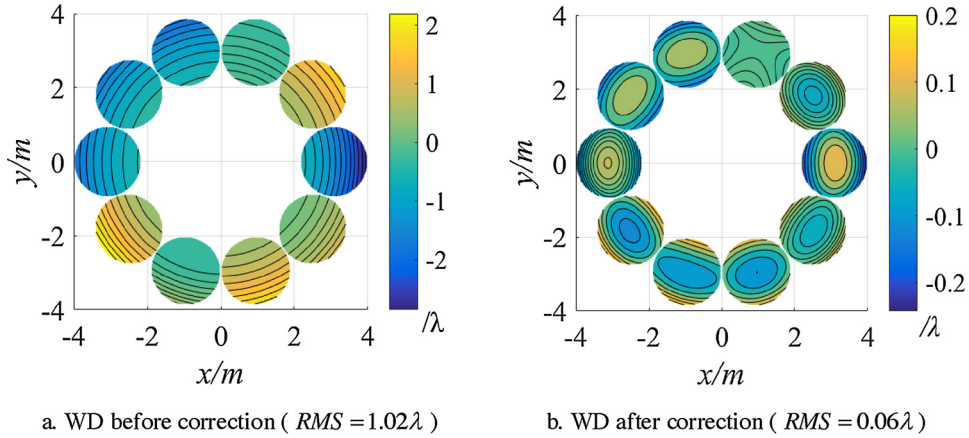


Fig. 8. Correction of the WD originating from segment with different prescription errors.

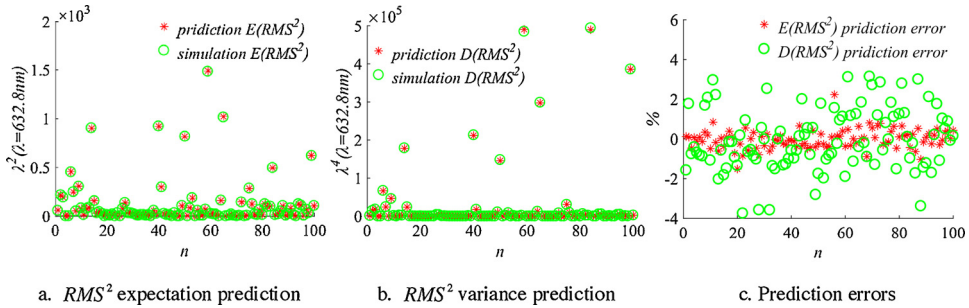


Fig. 9. Verification results of 100 random sampling for the residual wavefront deformation.

are less than $\pm 2\%$ and $\pm 5\%$ respectively. Moreover, the samples are highly discrete, and some sampling results are much larger than the other samples, but the predictions are still ideal, which indicates that the prediction method we propose is universally valid.

5. Conclusion

This paper proposed the calculation method of the linear sensitivity matrix of the WD originating from segments prescription errors, derived the prediction formula of the WD stemming from the random segments prescription errors, presented the correction and prediction method that using segment pose adjustment compensates prescription errors, and achieved plenty of Monte Carlo simulations. Our research reveals that the random prescription errors will lead to uncertain WD, which approximately follows the chi-square distribution and can be predicted using the method proposed in this paper. Its prediction errors of RMS^2 expectation and variance are less than $\pm 2\%$ and $\pm 5\%$ respectively. The WD originating from segments prescription errors can be effectively compensated by the segments pose adjustment. The compensation effect is better than one order of magnitude, but there will still be residual WD left, which also obeys the chi-square distribution and can be predicted using the method proposed in this paper. The prediction accuracy is the same as that of the prescription errors.

Funding

This work was supported by the National Key Technologies R&D Program of China (Grant No. 2016YFB0500100), Civil aerospace pre-research project (Grant No. D040101), Equipment pre-research project (Grant No. 30502010501HT01), National Natural Science Foundation of China (Grant No. 11873007).

References

- [1] J.M. Oschmann, M. Clampin, H. MacEwen, Special section guest editorial: space telescopes, *Opt. Eng.* 52 (2013) 091801, , <https://doi.org/10.1117/1.OE.52.9.091801>.
- [2] J.S. Fender, Future trends in large space optics, *Proc. SPIE* 4013 (2000) 682–686, <https://doi.org/10.1117/12.394005>.
- [3] N. Rioux, H. Thronson, L. Feinberg, H.P. Stahl, D. Redding, A. Jones, J. Sturm, C. Collins, A. Liu, A future large-aperture UVOIR space observatory: reference designs, *Proc. SPIE* 9602 (2015) 960205, , <https://doi.org/10.1117/12.2187758>.
- [4] D.C. Redding, L. Feinberg, M. Postman, H.P. Stahl, C. Stahle, H. Thronson, Beyond JWST: performance requirements for a future large UVOIR space telescope, *Proc. SPIE* 9143 (2014) 914312, , <https://doi.org/10.1117/12.2056568>.
- [5] C.F. Lillie, Large deployable telescopes for future space observatories, *Proc. SPIE* 5899 (2005) 58990D, , <https://doi.org/10.1117/12.624231>.
- [6] H.P. Stahl, H. Thronson, S. Langhoff, M. Postman, D. Lester, C.F. Lillie, R.J. Brissenden, Potential astrophysics science missions enabled by NASA's planned Ares V, *Proc. SPIE* 7436 (2009) 743607, , <https://doi.org/10.1117/12.826748>.
- [7] H.S. Yang, X.J. Zhang, Z.L. Li, H. Bao, Y.C. Fan, Technology and development of deployable segmented ultra-large-aperture space remote sensors, *Opt. Precis. Eng.* 26 (2018) 1287–1298.
- [8] C. Atkinson, S. Texter, R. Keski-Kuha, L. Feinberg, Status of the JWST optical telescope element, *Proc. SPIE* 9904 (2016) 990403, , <https://doi.org/10.1117/12.927594>.
- [9] M. Postman, T. Brown, K. Sembach, M. Giavalisco, W. Traub, K. Stapelfeldt, D. Calzetti, W. Oegerle, R.M. Rich, H.P. Stahl, J. Tumlinson, M. Mountain, R. Soummer, T. Hyde, Advanced technology large-aperture space telescope: science drivers and technology developments, *Opt. Eng.* 51 (2012) 011007, , <https://doi.org/10.1117/1.OE.51.1.011007>.
- [10] J.J. Rey, A. Wirth, A. Jankevics, F. Landers, D. Rohweller, C.B. Chen, A. Bronowicki, A deployable, annular, 30m telescope, space-based observatory, *Proc. SPIE* 9143 (2014) 914318, , <https://doi.org/10.1117/12.2057182>.
- [11] A. Jacob, P. Parihar, A co-phasing technique for segmented mirror telescopes, *Proc. SPIE* 9654 (2015) 96540G, , <https://doi.org/10.1117/12.2181778>.
- [12] D. Yue, S.Y. Xu, H.T. Nie, Co-phasing of the segmented mirror and image retrieval based on phase diversity using a modified algorithm, *Appl. Opt.* 54 (2015) 7917–7924, <https://doi.org/10.1364/AO.54.007917>.
- [13] H. Choi, I. Trumper, M. Dubin, W.C. Zhao, D.W. Kim, Simultaneous multi-segmented mirror orientation test system using a digital aperture based on sheared Fourier analysis, *Opt. Express* 25 (2017) 18152–18164, <https://doi.org/10.1364/OE.25.018152>.
- [14] Z. Liao, Q. Qui, H. Xian, Self-calibrating phase measurement based on diffraction theory and numerical simulation experiments, *Opt. Eng.* 54 (2015) 025116, , <https://doi.org/10.1117/1.OE.54.2.025116>.
- [15] K.N. Yao, J.L. Wang, X.Y. Liu, H.W. Li, M.H. Wang, B.C. Cui, S.H. Yu, Pyramid wavefront sensor using a sequential operation method, *Appl. Opt.* 54 (2015) 3894–3901, <https://doi.org/10.1364/AO.54.003894>.
- [16] J.L. Jiang, W.R. Zhao, Phasing piston error in segmented telescopes, *Opt. Express* 24 (2016) 19123–19137, <https://doi.org/10.1364/OE.24.019123>.
- [17] J.F. Simar, Y. Stockman, J. Surdej, Single-wavelength coarse phasing in segmented telescopes, *Appl. Opt.* 54 (2015) 1118–1123, <https://doi.org/10.1364/AO.54.001118>.
- [18] G.H. Ju, C.X. Yan, Z.Y. Gu, Elimination of the field-dependent aberrations of the JWST-like space telescopes in the multi-field fine-phasing process, *Appl. Opt.* 56 (2017) 2724–2740, <https://doi.org/10.1364/AO.56.002724>.
- [19] G. Chanan, M. Troy, Strehl ratio and modulation transfer function for segmented mirror telescopes as functions of segment phase error, *Appl. Opt.* 38 (1999) 6642–6647, <https://doi.org/10.1364/AO.38.006642>.
- [20] J.L. Flores, M. Strojnik, G. Pa'ez, G. Garcí'a-Torales, Effects of misalignment error on the optical transfer functions of synthetic aperture telescopes, *Appl. Opt.* 43 (2004) 5926–5932, <https://doi.org/10.1364/AO.43.005926>.
- [21] J. Zhang, W.R. Zhao, F. Yang, L.F. Zhang, The effects of piston error on image quality of synthetical aperture optical imaging system, *Proc. SPIE* 8557 (2012) 85570Z, , <https://doi.org/10.1117/12.999733>.
- [22] Z. Liu, S.Q. Wang, L.H. Huang, C.H. Rao, Analysis of relationship between far-field images and piston error of synthetic-aperture telescopes for the broadband target wave, *Proc. IEEE-2010 OSA-IEEE-Cos Advances in Optoelectronics and Micro/Nano-Optics* (2011) 1–5, <https://doi.org/10.1109/AOM.2010.5713589>.
- [23] D.C. Redding, W.G. Breckenridge, Optical modeling for dynamics and control analysis, *J. Guid. Control Dyn.* 14 (1991) 1021–1032, <https://doi.org/10.2514/3.20745>.
- [24] K. Yuan, P.M. Bentler, Two simple approximations to the distributions of quadratic forms, *Br. J. Math. Stat. Psychol.* 63 (2010) 273–291, <https://doi.org/10.1348/000711009X449771>.